symmetry

MDPI

Article

A Symmetry-Coordinated Approach for Ionospheric Modeling: The SH-RBF Hybrid Model

Hongmei Yi, Xusheng Zhang * and Wenbin Deng *

College of Civil Engineering and Architecture, Xinjiang University, Urumqi 830017, China; 005346@xju.edu.cn
* Correspondence: zxs1373018@163.com (X.Z.); dwb@xju.edu.cn (W.D.)

Abstract

Ionospheric delay errors significantly reduce the positioning accuracy of global navigation satellite systems (GNSSs), whereas precise ionospheric modeling can effectively mitigate this issue. The ionosphere exhibits large-scale symmetry, and spherical harmonics (SHs) can effectively describe this property due to their rotational symmetry on the sphere. However, mathematical fitting models such as spherical harmonic functions and polynomial models encounter boundary inaccuracies caused by edge effects. To address this problem, we developed a spherical harmonic–radial basis function (SH-RBF) hybrid method based on the integration of spherical harmonics and radial basis function interpolation techniques. This method leverages the global symmetry of spherical harmonics and utilizes the local adaptability of radial basis functions to correct regional distortions. Validation using European GNSS data during both geomagnetically quiet and active periods, in comparison with the CODE global ionospheric map (GIM), demonstrates that the modeling accuracy of spherical harmonics surpasses that of POLY during geomagnetically quiet periods. Compared to spherical harmonics, SH-RBF improves overall modeling accuracy by 8.87–27.27% and enhances accuracy in edge regions by 34.16–83.91%. During geomagnetically active periods, the SH-RBF method also achieves notable improvements. This study confirms that SH-RBF is a reliable technique for significantly reducing edge effects in regional ionospheric modeling.

Keywords: ionospheric model; GNSS; radial basis function interpolation; spherical harmonic function; SH-RBF

Check for updates

Academic Editors: Pedro Vega-Jorquera and Sergio Luiz E. F. da Silva

Received: 10 October 2025
Revised: 11 November 2025
Accepted: 1 December 2025
Published: 1 January 2026

Copyright: © 2026 by the authors. Licensee MDPI, Basel, Switzerland. This article is an open access article distributed under the terms and conditions of the Creative Commons Attribution (CC BY) license.

1. Introduction

The ionosphere is the atmospheric layer extending from 60 to 2000 km in altitude, and it induces a significant error known as the ionospheric delay in Global Navigation Satellite Systems (GNSSs). As a dispersive medium, it alters the speed and curvature of GNSS signal paths, resulting in ranging errors that can reach from tens to hundreds of meters [1]. To mitigate these effects and enhance positioning accuracy, the incorporation of a Total Electron Content (TEC) model is essential [2]. With the rapid development of multi-system GNSSs, the multi-mode and multi-frequency GNSS observation capability has been gradually formed, providing more observation data for GNSS ionospheric monitoring and modeling [3,4].

Over the past few decades, numerous scholars have proposed various modeling approaches, such as polynomial models [5], trigonometric models [6], and spherical harmonic models [7]. Subsequently, these models underwent further development. Building upon the triangular model, Yuan et al. introduced the Ionospheric Eclipse Factor (IEF) and

its influencing factors based on the Ionospheric Puncture Point (IPP), proposing an IEF method [8]. This approach enables precise differentiation between daytime and nighttime ionospheric conditions and effectively integrates them across different seasons. J.R.K. Kumar Dabbakuti proposed a regional ionospheric delay correction method based on the Adjusted Spherical Harmonic Function (ASHF) model. The ASHF model improved the ionospheric time delay corrections by 12.98% relative to the Klobuchar model [9]; Liu Ang et al. proposed the Spherical Harmonic Adjustment Overlay Kriging (SHAKING) method for real-time modeling of regional vertical total electron content (VTEC), demonstrating significant advantages over modeling methods like IDW [10]. Cheng et al. [11] introduced a novel piecewise linear transformation adjusted spherical crown harmonic (PLT-ASCH) method to mitigate local accuracy degradation across different latitudes under active and stable ionospheric conditions. To improve the positioning accuracy for single-frequency GNSS users in low-latitude regions, Ana L. Christovam et al. [12] investigated the capability of calculating ionospheric corrections in the form of regional ionospheric maps using only the GPS L1 frequency, and demonstrated the feasibility of developing ionospheric models and improving positioning in low-latitude areas with single-frequency GNSS data. Differential code bias (DCB) has a significant impact on ionospheric modeling. To accurately correct receiver DCB, Bo-Wen Xiong et al. [13] studied different receiver DCB correction methods, showing that the ionospheric delay modeling accuracy reached its optimal level when using the single-epoch RDCB correction strategy. Yang Junling et al. [14] proposed a new ionospheric modeling method that improves both the timeliness and accuracy of PPP-RTK corrections. This method introduces a linear fitting function to estimate user-specific residuals for compensation, and compared with traditional coordinate-based polynomial approaches, it significantly enhances fitting accuracy under high ionospheric activity. In recent years, with the rise of machine learning, researchers have increasingly applied neural network models to ionospheric modeling and prediction. Ju-Min Zhao et al. [15] employed the XGBoost algorithm and temporal convolutional networks to study ionospheric TEC at different latitudes in China. Kaselimi et al. [16] utilized LSTM and recurrent neural network (RNN) methods for TEC modeling and forecasting. Jun Tang et al. [17] successfully predicted ionospheric TEC using the GRU mechanism. To further improve the accuracy of ionospheric forecasts, researchers have integrated various algorithms with neural network models and proposed models such as WOA-CNN-LSTM [18] and BiLSTM-GRU-Attention [19], all of which have achieved favorable results.

Four commonly used methods in ionospheric modeling include direct data interpolation, data-driven empirical models (DEMs), three-dimensional ionospheric tomography, and mathematical function fitting [20–23]. The characteristics of these methods are as follows: (1) Direct data interpolation relies heavily on the distribution of ionospheric pierce points (IPPs), resulting in low accuracy in regions with sparse or missing observation data; (2) Empirical models can provide background ionospheric information but require a large amount of external data input; (3) Ionospheric tomography enables three-dimensional characterization of the vertical electron density structure but requires more complex algorithms and higher computational demands; (4) Mathematical fitting methods possess clear mathematical structures and partial physical interpretability, facilitating the elucidation of ionospheric variation mechanisms. However, mathematical fitting methods struggle to fully capture ionospheric disturbances driven by specific geophysical processes, such as those related to acoustic gravity waves (AGWs) [24], which introduce meso- and small-scale structures that are not effectively represented by smooth basis functions. In addition, projection errors on the Earth's surface can trigger edge effects, significantly reducing accuracy at the boundaries of the modeled region. Although methods such as SHAKING and PLT-ASCH can effectively alleviate accuracy loss, correcting edge distortions

remains challenging due to uneven station distribution and the incomplete symmetry of the ionosphere, warranting further investigation.

To directly correct edge distortions and further improve ionospheric modeling accuracy, we propose the spherical harmonic–radial basis function interpolation (SH-RBF) method. This method combines the global characterization capability of spherical harmonics with the local correction capability of radial basis interpolation, applying spherical harmonic functions to model the overall ionosphere in specific regions, while radial basis function interpolation is specifically employed to estimate and correct errors in low-accuracy edge regions. In this study, GNSS observation data from selected regions in Europe are used to establish a regional ionospheric model based on SH-RBF. By comparing the accuracy of polynomial models, spherical harmonic models, and SH-RBF models with the ionospheric grid maps provided by the European Center for Orbit Determination (CODE), a comprehensive analysis is conducted.

In the following, the method of ionospheric modeling and DCB estimation is described in detail in Section 2, alongside the collection of GNSS observation data across varying geomagnetic conditions. Section 3 presents a visualization of the SH-RBF modeling results, with their accuracy validated against ionospheric data from the International GNSS Service (IGS). The relationship between the optimal order of spherical harmonics and the geomagnetic environment is investigated in Section 4. Finally, the corresponding conclusions are provided in Section 5.

2. Methods and Data

2.1. Ionospheric Modeling Methods

2.1.1. Ionospheric Delay Extraction

GNSS signals currently primarily consist of two fundamental measurements: pseudorange and carrier phase. Their observation equations are as follows [25]:

$$P_j^k = \rho_j^k + I_j^k + V_{j,trop}^k + c(dt_r - dt^s) + (d^k - d_r) + \varepsilon_{P,J}^k \tag{1}$$

$$\phi_j^k \cdot \lambda = \rho_j^k - I_j^k + V_{j,trop}^k + c(dt_r - dt^s) + N_j^k \lambda_j + (b^k - b_r) + \varepsilon_{P,J}^k \tag{2}$$

Here, P denotes the GNSS pseudorange observation, ϕ represents the GNSS carrier phase observation, ρ indicates the geometric distance between the satellite and receiver, k is the satellite index, j denotes the frequency, I represents the ionospheric delay, $V_{j,trop}$ denotes tropospheric delay, c represents the speed of light in vacuum, dt^s signifies satellite clock offset, dt_r indicates receiver clock offset, d denotes hardware delay in ranging codes for satellite and receiver, b represents hardware delay in carrier phase for satellite and receiver, λ is wavelength, N is the satellite carrier phase ambiguity parameter, and ε denotes white noise in observations.

Ionospheric delay can be expressed as:

$$I_j = 40.28 \times \frac{STEC}{f_j^2} \tag{3}$$

STEC denotes the Slant Total Electron Content (STEC) along the satellite signal propagation path, measured in TECu, where 1 TECu = 10^{16} electrons/m^2. The letter f represents the frequency corresponding to the satellite signal.

The ionospheric delay expression obtained by dual-frequency carrier phase smoothing pseudo range acquisition is:

$$STEC = -\frac{f_1^2 f_2^2}{40.28(f_1^2 - f_2^2)}(P_{4,sm} - cDCB^S - cDCB_r) \tag{4}$$

In the equation, $P_{4,sm}$ is the carrier-smoothed pseudorange observation value. Converting the total electron content (STEC) to the zenith direction (VTEC), which is independent of the elevation angle, can directly reflect the overall characteristics of the ionosphere above the measuring station. The projection function used is

$$F(z) = \frac{1}{\sqrt{1 - \left(\frac{R_c}{R_c+H}\sin(\alpha \cdot z)^2\right)}} \tag{5}$$

where z is the zenith distance in the direction of the measuring station; R_c represents the average radius of the Earth, R_c = 6371 km; H is the single-layer height of the ionosphere, which is taken as 450 km in this paper; α is the zenith distance coefficient, α = 0.9782 [26,27].

2.1.2. Polynomial Models

The Polynomial Model (POLY) is a mathematical approach for describing the Vertical Total Electron Content in the ionosphere. It employs a set of polynomial functions to approximate the VTEC distribution, representing VTEC as a function of latitude difference and solar hour angle difference. This approach is essentially an algebraic expansion based on a local reference plane defined by latitude and longitude offsets, and as such, it implicitly relies on a form of local planar symmetry—specifically, the translational and mirror symmetries inherent to a Cartesian coordinate system. The mathematical expression is shown in Equation (6):

$$VTEC(\alpha, \beta) = \sum_{a=0}^{n}\sum_{b=0}^{m} E_{ab}(\alpha - \alpha_0)^a(\beta - \beta_0)^b \tag{6}$$

Among these, E_{ab} represents the estimated model coefficients for the polynomial function, with n and m denoting the maximum order of the model; α and β denote the latitude and longitude of the ionospheric piercing point, while α_0 and β_0 denote the latitude and longitude of the observation area's center point, all within the geocentric geomagnetic coordinate system.

2.1.3. Spherical Harmonic Function Model

The ionosphere, as a layer enveloping the Earth, exhibits large-scale structures that possess inherent symmetries, particularly rotational symmetry on a sphere. Spherical harmonics (SHs) are the natural mathematical tool to describe such symmetric physical fields. They form a complete set of orthogonal basis functions that are the eigenfunctions of the angular part of Laplace's equation in spherical coordinates. This fundamental connection to the Laplace equation endows SH with profound rotational symmetry properties, making them ideal for representing any square-integrable function on a sphere. The VTEC expression based on spherical harmonics is shown in Equation (7):

$$VTEC(\varphi, \lambda) = \sum_{n=0}^{n_{\max}}\sum_{m=0}^{n} \widetilde{P}_{nm}(\sin\varphi)[O_{nm}\cos(m\lambda) + Q_{nm}\sin(m\lambda)] \tag{7}$$

In this equation, m is the order of the spherical harmonic expansion, $n_{\max}$ is the maximum order of the expansion, φ and λ are the latitude and longitude of the ionosphere IPP, respectively. O_{nm} and Q_{nm} are the parameters to be determined, and $\widetilde{P}_{nm}$ is the nth-order mth-degree normalized Legendre polynomial function.

2.1.4. SH-RBF Model

Due to the influence of Earth projection errors, relying solely on spherical harmonics during ionospheric modeling may result in suboptimal modeling performance in marginal regions. To enhance ionospheric modeling quality and mitigate the impact of edge effects, this paper proposes the SH-RBF method: spherical harmonics are primarily employed to fit the TEC of the regional ionosphere, while residual corrections are applied to less accurate marginal regions through radial basis function interpolation, as shown below:

$$I(\varphi,\lambda) = SH(\varphi,\lambda) + RBF(\varphi,\lambda) \tag{8}$$

$$SH(\varphi,\lambda) = \sum_{n=0}^{n_{\max}} \sum_{m=0}^{n} \widetilde{P}_{nm}(\sin\varphi)[O_{nm}\cos(m\lambda) + Q_{nm}\sin(m\lambda)] \tag{9}$$

$$RBF(\varphi,\lambda) = \left| \sum_{i=1}^{n} c_i B(h_{ij}) \right| \tag{10}$$

In the above expression, $I(\varphi,\lambda)$ represents the VTEC value of the ionosphere, and $RBF(\varphi,\lambda)$ denotes the residual correction value calculated using RBF interpolation in the boundary, φ represents latitude, and λ represents longitude.

The radial basis function (RBF) method is a widely used mathematical approach for addressing problems in geophysics, surveying, topography, and hydrology, particularly in interpolation and machine learning [28]. The RBF method possesses robust nonlinear modeling capabilities, enabling it to capture complex nonlinear relationships by adjusting the parameters of the basis functions.

The specific implementation procedure of the SH-RBF algorithm is as follows: First, an initial spherical harmonic function model is established using all GNSS observation data within the study area to obtain the background global VTEC distribution. To accurately identify regions affected by boundary effects, this study adopts a data-driven dynamic boundary identification strategy. At each modeling epoch, the absolute residuals at all observation points are computed, and the top 25% of observations with the largest residuals are selected as high-residual samples. The spatial extent corresponding to these samples is defined as the "boundary region" for that epoch. These high-residual points are predominantly distributed along the periphery of the study area, validating the effectiveness of this identification method.

In this study, we selected the multiquadric (MQ) function as the interpolation kernel from the various radial basis functions (RBFs) proposed by Hardy in 1971 [29]. This choice was based on the widely recognized superior interpolation performance of the MQ function when handling spatially scattered data [30]. The MQ function introduces a shape parameter (R^2), which provides additional flexibility and allows us to adjust the curvature of the function according to the characteristic scale of ionospheric disturbances. This enables an optimal balance between smoothness and local adaptability in the fitting process.

The Radial Basis Function interpolation method employed in this study inherently exhibits a distinct form of symmetry—radial symmetry. The value of the Multiquadric basis function at any given point depends solely on its Euclidean distance to the center point, endowing it with complete isotropy. Within the SH-RBF framework, while the Spherical Harmonics capture the global rotational symmetry of the ionospheric shell, the RBF interpolation addresses local distortions utilizing its intrinsic local radial symmetry, thereby enhancing the overall accuracy of the ionospheric model.

In MQ interpolation, for each given reference point, a function of the form $B_i(x,y)$ is used. Use function $f(x,y) = \sum_{i=1}^{n} c_i B_i(x,y)$ to calculate the weight coefficients. The most commonly used function type for $B_i(x,y)$ is the univariate radial function. To achieve this,

a radial function of the form $B_i(x,y) = B(h_i)$ is employed, where hi denotes the distance between two points. The accuracy of the multiple quadratic surface method is determined by the shape parameter R^2. The smoothness of the interpolation can be influenced by the shape parameter R^2, which is selected based on the given circumstances.

$$h_i = \sqrt{(x - x_i)^2 + (y - y_i)^2} \tag{11}$$

$$B(h_i) = \sqrt{h_i^2 + R^2} \tag{12}$$

$$z = \sum_{i=1}^{n} c_i B(h_i) \tag{13}$$

Here, h_i denotes the Euclidean distance between two points, R^2 is the shape parameter, and several suggested values for R^2 can be found in the literature [31–33]. To achieve optimal interpolation accuracy, this study did not use fixed empirical values. Instead, we determined the optimal shape parameter by iteratively searching through multiple predefined candidates. For a multi-quadric surface with n given data points, assuming the MQ basis functions pass through these points, the following formula can be derived:

$$z_j = \sum_{i=1}^{n} c_i B(h_{ij}) \quad j = 1, 2, \ldots, n \tag{14}$$

$$h_{ij} = \sqrt{(x_j - x_i)^2 + (y_j - y_i)^2} \tag{15}$$

$$B(h_{ij}) = \sqrt{h_{ij}^2 + R^2} \tag{16}$$

In the above expression, h_{ij} denotes the distance from the jth interpolation point to the ith data point, $B(h_{ij})$ represents the multi-quadratic radial basis function, c_i is an unknown coefficient, and z_j indicates the measured value at the jth data point. When these equations are transformed into a linear system, the following results are obtained:

$$\psi_c = z \tag{17}$$

The solution in matrix form is given by the following equation:

$$c = (\psi^T \psi)^{-1} \psi^T z \tag{18}$$

Among them, $\psi_{n\times n}$ is the basis function matrix, $c_{1\times n}$ is the unknown coefficient vector, $z_{1\times n}$ is the known vector, which can be defined as follows:

$$\psi_{n\times n} = \begin{bmatrix} B(h_{11}) & B(h_{12}) & \ldots & B(h_{1n}) \\ B(h_{21}) & B(h_{22}) & \ldots & B(h_{2n}) \\ \vdots & \vdots & \ddots & \vdots \\ B(h_{n1}) & B(h_{n2}) & \ldots & B(h_{nn}) \end{bmatrix}, c_{1\times n} = \begin{bmatrix} c_1 \\ c_2 \\ \vdots \\ c_n \end{bmatrix}, z_{1\times n} = \begin{bmatrix} z_1 \\ z_2 \\ \vdots \\ z_n \end{bmatrix} \tag{19}$$

After determining the unknown coefficients, calculate the estimated values of the interpolation points according to the following formula.

$$\hat{z}_j = \sum_{i=1}^{n} c_i B(h_{ij}) \tag{20}$$

2.1.5. Calculate Differential Code Bias

Differential code bias (DCB) affects the propagation of satellite signals and therefore must be eliminated during ionospheric modeling [34]. In this study, we assume that the DCBs at both the satellite and receiver ends remain constant throughout the day, and estimate them as unknown parameters alongside the ionospheric model parameters. However, during the estimation process, a linear correlation exists between satellite DCB and receiver DCB, making direct separation impossible and resulting in a rank-deficient normal equation. To address this rank deficiency, we adopted the general approach used by major international ionospheric analysis centers: a constraint is applied such that the sum of the DCBs for all satellites involved in the estimation on a given day is set to zero, providing a unique reference for the estimation. This constraint is equivalent to setting the mean DCB value of the entire satellite network to zero, thereby successfully separating satellite DCBs from receiver DCBs and obtaining their respective estimates.

2.2. Data

In this study, GNSS observation data from IGS stations in specific regions of Europe were used for modeling. The ionospheric modeling area covers latitudes from 45° N to 55° N and longitudes from 5° E to 30° E. Observation data were obtained from GPS, GLONASS, and Galileo systems, sampled at 30-s intervals. The temporal resolution was set to 2 h, and the spatial resolution was set to 5° in longitude and 2.5° in latitude. The elevation cutoff angle was set to 15°, and the ionospheric thin-layer height was assumed to be 450 km. Three methods were employed to model the ionosphere in this region: a 6th-order polynomial, a 6th-order spherical harmonic, and a 6th-order SH-RBF function. To verify the improvement achieved by the SH-RBF method, the selected stations are sparsely distributed at the edges of the study area. The distribution of observation stations is shown in Figure 1.

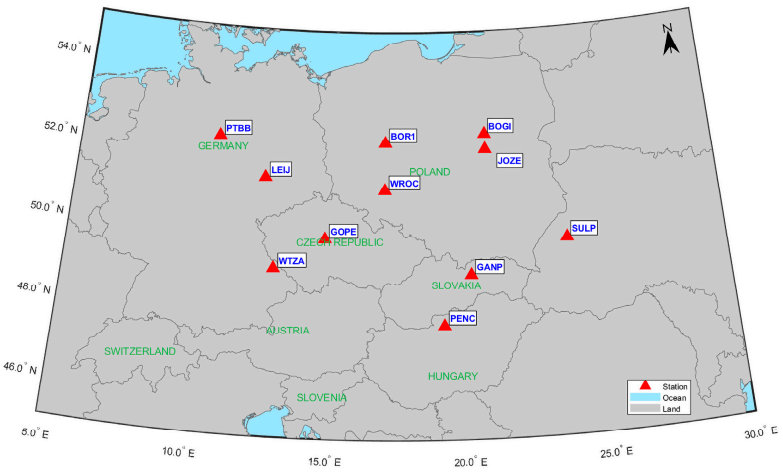


Figure 1. Geographic distribution map of monitoring stations in the study area.

Ionospheric activity is influenced by geomagnetic activity. Currently, indices such as the Dst index and Kp index are used to characterize geomagnetic activity. Data for the Dst index and Kp index are provided by the Space Environment Prediction Center (SEPC). The Dst index is a key indicator for measuring the intensity of geomagnetic storms. When the Dst value is between −50 and −30 nT, it is classified as a minor geomagnetic storm; when the Dst value is between −100 and −50 nT, it is classified as a moderate geomagnetic storm; and when the Dst value is between −200 and −100 nT, it is classified as a major geomagnetic storm. When the Kp value is between 5 and 6, it is classified as a moderate

to small geomagnetic storm, and when the Kp value exceeds 6, it is classified as a major geomagnetic storm.

To verify the reliability of the SH-RBF model during both geomagnetically active and quiet periods, this study selected a total of 14 days of GNSS observation data for ionospheric modeling, covering the periods from 11 May to 17 May 2019, and from 29 September to 5 October 2019.

Figure 2 presents the Dst and Kp indices from May 9 to 19 and from September 27 to 6 October 2019. On 14 May 2019, the Dst index exceeded −60 nT and the Kp index reached 7, indicating the occurrence of a geomagnetic storm accompanied by intense geomagnetic activity. On 2 October 2019, the Dst index did not exceed −20 nT and the Kp index remained below 3. Therefore, 2 October 2019, was classified as a geomagnetically quiet period. This paper provides a detailed analysis of ionospheric variations and accuracy on 14 May and 2 October 2019.

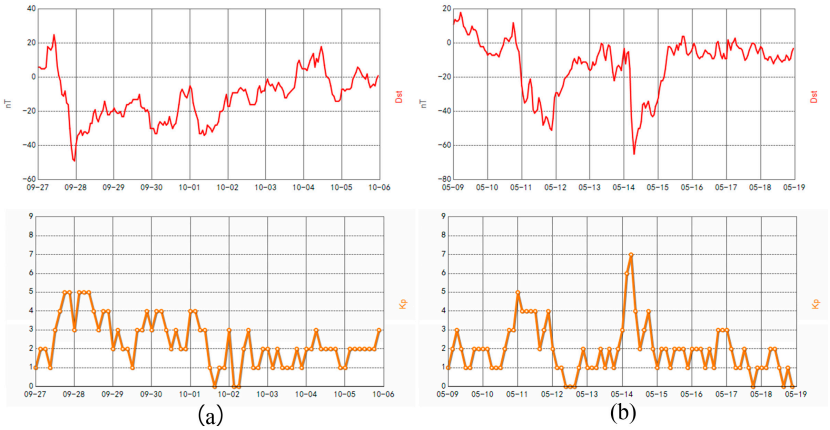


Figure 2. Statistical chart of geomagnetic activity. (**a**) geomagnetically quiet periods. (**b**) geomagnetically active periods.

3. Results

3.1. Modeling Results

3.1.1. Geomagnetically Quiet Periods

Figure 3 presents a comparison between the satellite DCBs estimated during geomagnetically quiet periods and the corresponding IGS final products for 32 satellites. The deviations for all satellites ranged from 0 to 0.48 ns, with the majority being below 0.2 ns. The overall mean deviation was approximately 0.17 ns, demonstrating the high accuracy of the DCB estimates.

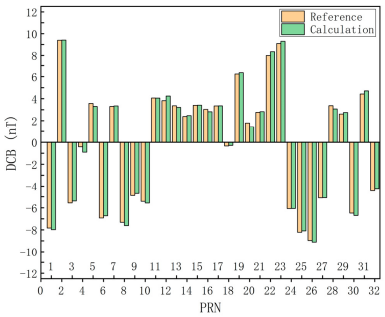


Figure 3. Comparison of Satellite-Side DCB Results from Modeling and Computation vs. IGS Release (2 October 2019).

In this study, satellite and receiver DCB were solved simultaneously. To prevent satellite DCB from transferring to receiver DCB, the modeled DCB of selected ground

IGS stations was compared with the station DCB released by the IGS Data Center. The results are shown in Figure 4. The DCBs calculated for most stations exhibit minimal deviation from the IGS-published values. Calculations indicate an average DCB error of approximately 1.19 for these stations, reflecting a low overall error rate. This confirms the high accuracy of the DCB solution process.

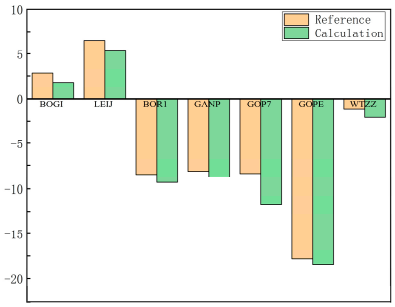


Figure 4. Comparison of DCB from modeling and calculation at selected ground stations with IGS-published DCB (2 October 2019).

The ionosphere above Earth is primarily generated by solar radiation. Since solar radiation varies across different regions of Earth at different times of the day, the state of the ionosphere also fluctuates accordingly. To accurately describe the temporal evolution of the ionosphere, this study divides a 24 h period into 12 time points, performing ionospheric modeling every 2 h.

The ionospheric TEC variations derived from the SH-RBF model during a geomagnetically quiet day are presented in Figure 5. The model successfully captures the characteristic diurnal pattern, revealing a significant increase in ionization between 10:00 and 16:00. The TEC reached its maximum value of 11.39 TECu at approximately 14:00, which aligns with the expected peak in solar radiation intensity. This well-defined and smooth diurnal variation, characterized by a single prominent peak, is typical of ionospheric behavior under undisturbed conditions and provides a baseline against which disturbed-period dynamics can be contrasted.

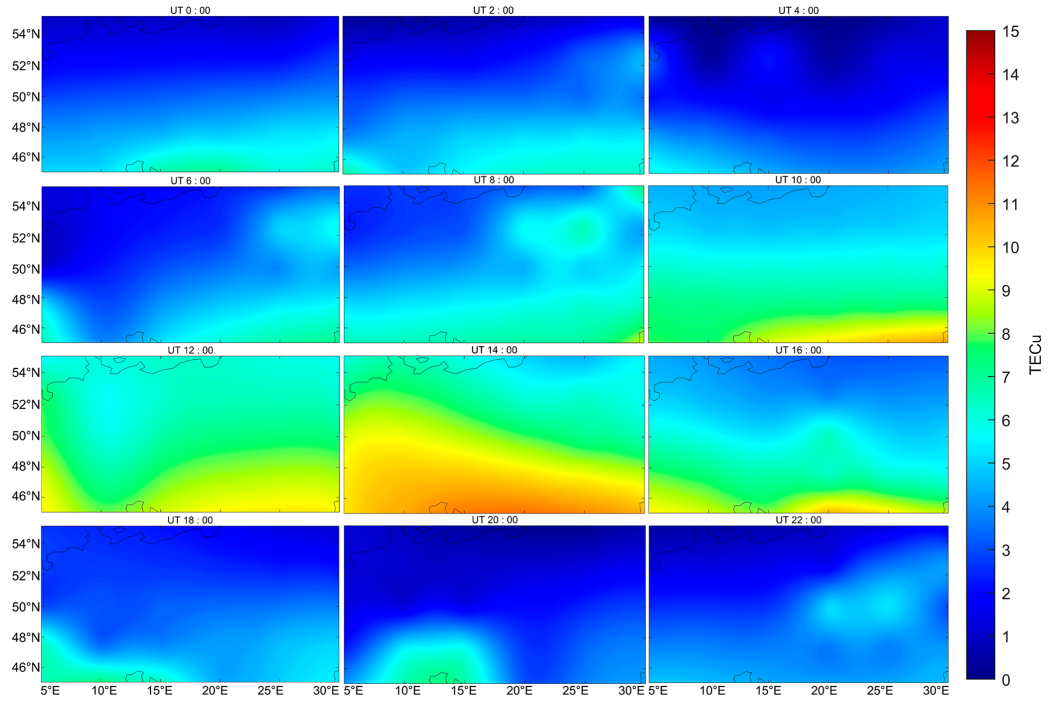


Figure 5. SH-RBF Ionospheric Modeling Results During Geomagnetically Quiet Periods.

3.1.2. Geomagnetically Active Periods

A comparison between the satellite DCBs estimated during geomagnetically active periods and the official products released by the International GNSS Service is presented in Figure 6. The results show that the deviations for most satellites were below 0.5 ns, with only one satellite exhibiting a slightly larger deviation of 0.507 ns. The mean deviation across all satellites was 0.24 ns, demonstrating the high accuracy of the DCB estimation method employed in this study.

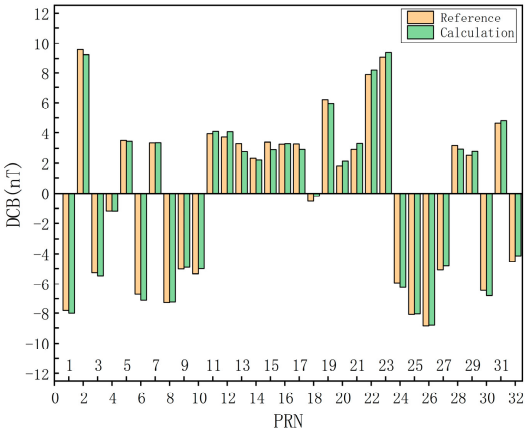


Figure 6. Comparison of Satellite-Side DCB Results from Modeling and Computation vs. IGS Release (14 May 2019).

A comparison was conducted between the DCBs of selected ground stations derived from modeling calculations and the station DCBs released by the IGS Data Center. The results are shown in Figure 7. For most stations, the DCBs obtained through modeling exhibited minimal deviation from the IGS-released DCBs. Calculations indicate that the average error in these stations' DCBs was approximately 0.42, representing a low overall error rate. This demonstrates that the overall accuracy of the DCB solution is high.

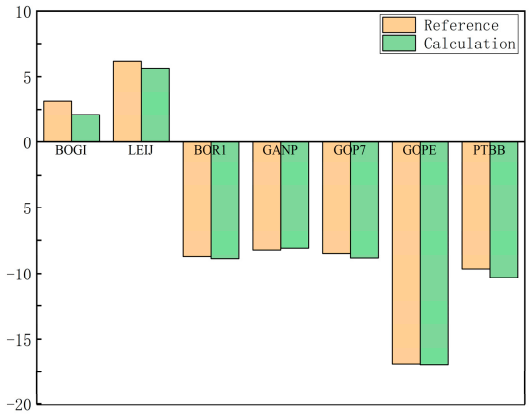


Figure 7. Comparison of DCB from modeling and calculation at selected ground stations with IGS-published DCB (14 May 2019).

The ionospheric modeling results for the geomagnetically active period (SH-RBF) are shown in Figure 8. These results differ markedly from those of the geomagnetically quiet period. During the active period, the ionosphere exhibited exceptional activity from 08:00 to 18:00, with the duration of this activity far exceeding that observed during the geomagnetically quiet period. The peak total electron content (TEC) reached 14.32 TECu during this active period, surpassing the peak value recorded during the geomagnetically quiet period.

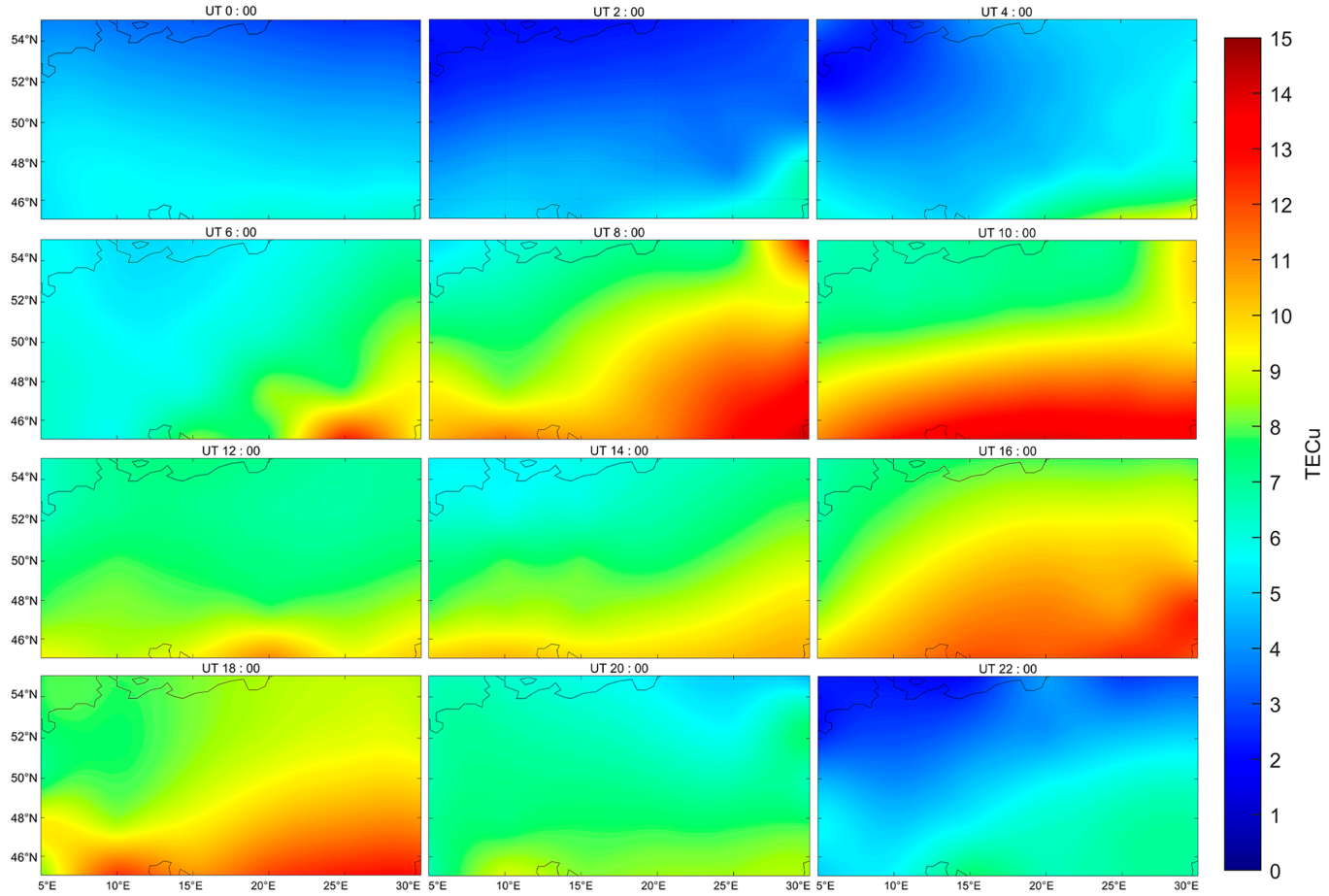


Figure 8. Visualization of SH-RBF Ionospheric Modeling During Geomagnetically Active Periods.

3.2. Accuracy Verification

The previous section validated the accuracy of the DCB estimated in this study, demonstrating good consistency. To further verify the modeling accuracy of the SH-RBF, this study compared the modeling accuracy of POLY, spherical harmonics, and SH-RBF by calculating the root mean square error (RMSE) and mean absolute error (MAE), using the GIM provided by CODE as a reference.

$$RMSE = \sqrt{\frac{\sum_{i=1}^{n} (VTEC_{g,i} - VTEC_{0,i})^2}{n}} \tag{21}$$

$$MAE = \frac{\sum_{i=1}^{n} \left| VTEC_{g,i} - VTEC_{0,i} \right|}{n} \tag{22}$$

In the equation, $VTEC_{g,i}$ denotes the i-th VTEC observation calculated using GIMs, $VTEC_{0,i}$ represents the i-th VTEC reference value, and n indicates the number of VTEC observations participating in the verification.

3.2.1. Geomagnetically Quiet Periods

Figure 9 shows the ionospheric TEC residual distribution maps based on the polynomial model, spherical harmonic function model, and SH-RBF model. Specifically, Figure 9a, Figure 9b, and Figure 9c correspond to the residual distribution results for the polynomial model, spherical harmonic function model, and SH-RBF model from 10:00 to 16:00, respec-

tively. Analysis indicates that compared to the polynomial and spherical harmonic models, the SH-RBF model exhibits higher modeling accuracy in boundary regions.

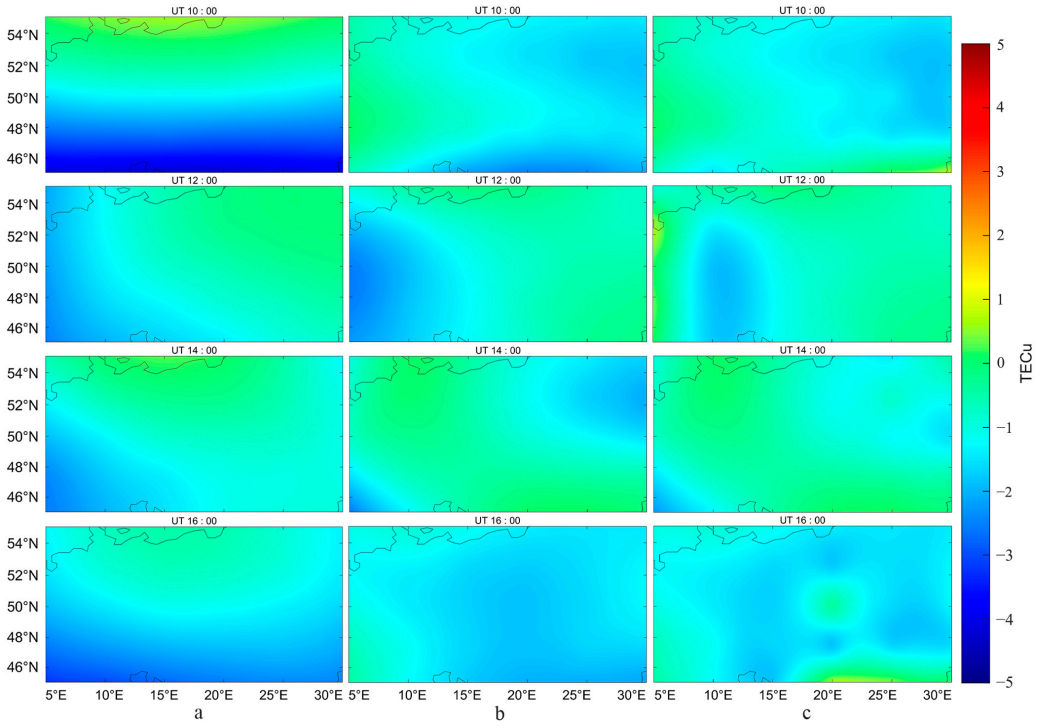


Figure 9. Residual Comparison Chart for the Geomagnetic Quiet Period from 10:00 to 16:00. (**a**) POLY. (**b**) SH. (**c**) SH-RBF.

The spatial distribution of residuals shows that during ionospheric peak periods, regions with high residuals are mainly concentrated at the southern edge of the study area. An important reason for this phenomenon is the sparse distribution of stations in the peripheral areas of the study region. For instance, in the southern area, there are only three stations: GANP, WTZA, and PENC, with distances between them exceeding 100 km. The strong adaptability of RBF interpolation to irregularly distributed data points enables it to maintain stable interpolation performance even in sparsely distributed boundary regions. As a result, the SH-RBF model significantly mitigates boundary errors.

Table 1 presents the RMSE values of different modeling methods at 14:00 UTC during the period from 29 September to 5 October 2019. As shown in Table 1, the SH-RBF function demonstrates notable improvements compared to the use of spherical harmonics alone. Subsequently, a detailed analysis is conducted for 2 October 2019.

To visually illustrate the modeling accuracy of POLY, spherical harmonics, and SH-RBF for the ionosphere, this study calculated the Mean Absolute Error (MAE) at each time point throughout a day during a geomagnetically quiet period. The results are shown in Figure 10. Compared to POLY, SH-RBF achieves a modeling accuracy improvement of 10.56% to 45.11%. Compared to using spherical harmonics alone, SH-RBF achieves a modeling accuracy improvement of 8.7% to 26.26%.

The RMSE statistics of the three models at 12 time points are shown in Table 2. Comparative analysis reveals that during geomagnetically quiet periods, the SH-RBF model achieved an overall modeling accuracy improvement of 8.87% to 27.27% compared to using spherical harmonics alone, with regional enhancements ranging from 34.16% to 83.91%. Compared to POLY, modeling accuracy improved by 6.98% to 51.03% overall and by 11.37% to 86.17% in boundary regions.

Table 1. RMSE Statistics at 14:00 UTC from 29 September to 5 October 2019.

DATE	Overall		Boundary	
	SH	SH-RBF	SH	SH-RBF
29 September	0.59	0.50	0.89	0.30
30 September	0.57	0.46	0.96	0.29
1 October	2.32	2.00	4.12	3.78
2 October	1.06	0.90	1.22	0.37
3 October	0.63	0.48	1.16	0.39
4 October	0.90	0.80	1.22	0.49
5 October	0.74	0.56	1.47	0.67

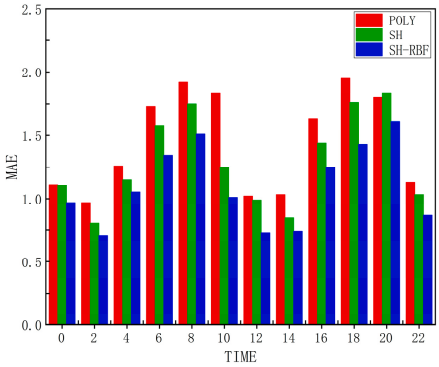


Figure 10. Statistical Chart of Average Absolute Error During Geomagnetically Quiet Periods.

Table 2. RMSE statistics for modeling accuracy of three models during geomagnetic quiet periods.

UT	Overall			Boundary		
	POLY	SH	SH-RBF	POLY	SH	SH-RBF
0	1.24	1.17	1.04	1.37	1.48	0.91
2	0.86	0.92	0.8	1.08	2.43	0.65
4	1.28	1.24	1.13	1.54	2.94	0.37
6	1.78	1.68	1.44	2.21	3.17	1.65
8	2.06	1.84	1.64	2.19	3.76	2.45
10	2.35	1.39	1.15	4.19	2.86	1.86
12	1.27	1.21	0.88	2.28	1.77	0.81
14	1.20	1.06	0.90	1.54	1.22	0.37
16	1.79	1.49	1.31	2.23	2.62	1.03
18	2.15	1.86	1.54	3.52	2.50	1.76
20	1.88	1.92	1.68	2.45	2.12	1.61
22	1.25	1.12	0.96	1.51	1.76	0.23

Due to the influence of solar radiation on the atmosphere, the errors of all models generally increase between 08:00 and 16:00 UTC. At specific time points such as 04:00 UTC, significant transitional gradients in ionospheric density are observed. The locally adaptive RBF correction is particularly effective in handling such rapid local variations. Consequently, the SH-RBF model exhibits a notable improvement in accuracy for edge regions at these time points, reaching over 80%.

3.2.2. Geomagnetically Active Periods

Figure 11 shows the distribution of ionospheric TEC residuals for three models during geomagnetically active periods. Figure 11a, Figure 11b, and Figure 11c correspond to the residual distributions of the polynomial model, spherical harmonic function model, and

SH-RBF model from 10:00 to 16:00, respectively. Comparison reveals that the SH-RBF model maintains high modeling accuracy even during geomagnetically active periods.

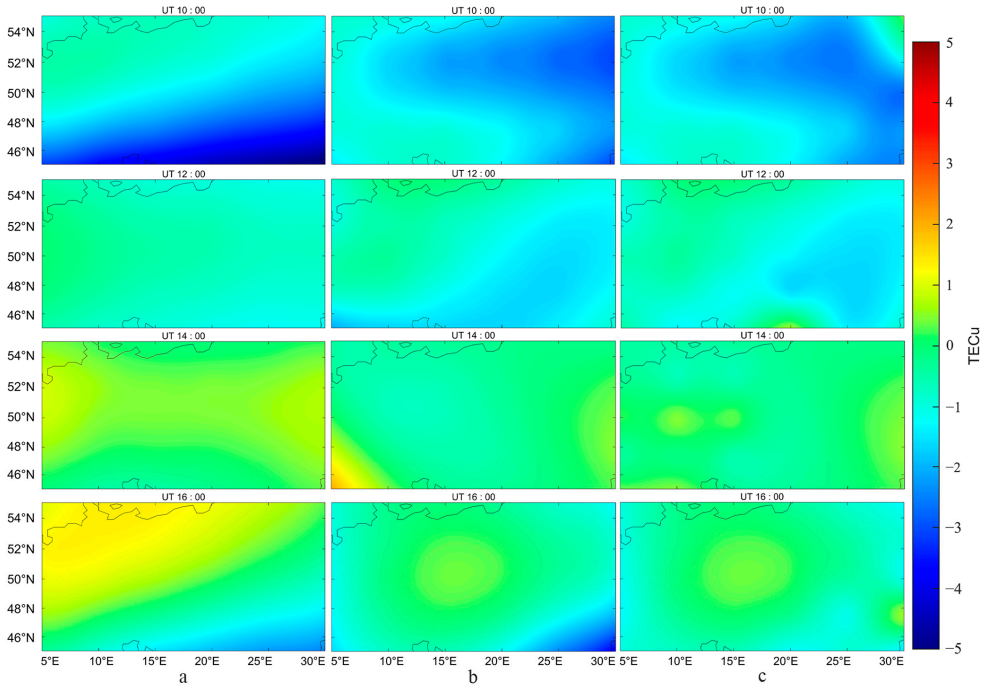


Figure 11. Residual Comparison Map for the Geomagnetically Active Period from 10:00 to 16:00. (**a**) POLY. (**b**) SH. (**c**) SH-RBF.

According to the residual distribution map, during periods of geomagnetic activity, the southern part of the study area is more significantly affected by geomagnetic disturbances. The "equatorial fountain effect" indirectly intensifies TEC fluctuations in this region. Additionally, as indicated by the filamentous and wavelike structures in Figure 11, acoustic-gravity waves (AGWs) also interfere with ionospheric activity. During geomagnetic storms, energy injected into high-latitude regions excites strong AGWs, which propagate toward lower latitudes and induce traveling disturbances in ionospheric electron density. These variations are difficult to fully capture using either spherical harmonics or radial basis function interpolation. Nevertheless, the SH-RBF model still demonstrates notable improvements in the edge regions of the study area. For example, between 10:00 and 16:00 UTC, the accuracy improvement in boundary regions achieved by SH-RBF compared to spherical harmonics ranges from 34.97% to 69.67%. Similarly, compared to the POLY method, the SH-RBF model also shows considerable enhancement in prediction accuracy for the edge regions.

Table 3 presents the root mean square error (RMSE) values at 14:00 UTC for different modeling methods during the period from 11 May to 17 May 2019. As shown in Table 3, the SH-RBF method still demonstrates significant improvement during geomagnetically active periods. Subsequently, a detailed analysis was conducted for 14 May 2019.

During periods of geomagnetic activity, the MAE of the three models at each time point is shown in Figure 12. Comparison results indicate that the ionospheric modeling accuracy of SH-RBF improved by 8.33% to 28.92% compared to spherical harmonics. Interestingly, at certain time points during geomagnetic activity, POLY's modeling accuracy surpassed that of SH-RBF. However, SH-RBF's average MAE over the entire day was 0.97, lower than POLY's daily MAE (1.03). This indicates that during geomagnetic activity, SH-RBF's modeling accuracy was overall slightly superior to POLY's.

Table 3. RMSE Statistics at 14:00 UTC for Each Day from 11 May to 17 May 2019.

DATE	Overall		Boundary	
	SH	SH-RBF	SH	SH-RBF
11 May	2.76	2.52	1.40	0.87
12 May	1.52	1.37	2.05	0.99
13 May	2.14	1.93	2.83	1.22
14 May	0.53	0.39	1.22	0.37
15 May	2.59	2.39	2.98	1.33
16 May	1.05	0.92	1.5	0.72
17 May	0.76	0.64	1.22	0.45

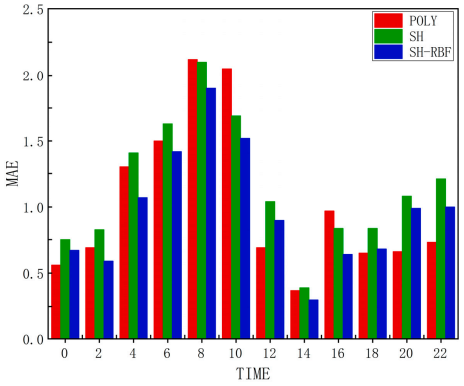


Figure 12. Statistical Chart of Average Absolute Error During Geomagnetically Active Periods.

Due to the combined effects of solar radiation and energy injection from geomagnetic storms, the spatial gradient of TEC increases significantly during 08:00–10:00 UTC. Both the POLY model and the SH model are unable to resolve such steep local gradients, resulting in an overall RMSE of 2.27 TECu and a boundary RMSE of 3.76 TECu at 08:00 UTC. By employing radial basis function interpolation, the SH-RBF model reduces the overall RMSE to 2.02 TECu and the boundary RMSE to 2.45 TECu.

Table 4 presents the root mean square error statistics for three models at different time intervals during geomagnetically active periods. Comparative analysis indicates that, compared to the spherical harmonic method alone, the SH-RBF model improves overall modeling accuracy by 8.06% to 36.93%, with particularly notable enhancement in boundary regions ranging from 24.06% to 86.41%. Although the SH-RBF performs excellently at the boundaries, during the most intense phase of the storm, the polynomial model may occasionally provide a better fit for large-scale structures in the central region that are severely disturbed. This suggests that while the current RBF interpolation is effective in handling edge effects, it may be influenced by the global disturbance background during extreme events, potentially leading to excessive smoothing or misrepresentation of certain storm-induced large-scale features. Nevertheless, the POLY model yields a full-day RMSE of 1.41 TECu, whereas the SH-RBF model achieves 1.19 TECu. Therefore, during geomagnetically active periods, the SH-RBF model demonstrates superior overall robustness compared to the POLY method.

Table 4. RMSE statistics for modeling accuracy of three models during periods of geomagnetic activity.

UT	Overall			Boundary		
	POLY	SH	SH-RBF	POLY	SH	SH-RBF
0	0.69	0.88	0.77	1.18	1.48	0.91
2	0.89	1.11	0.7	1.61	2.43	0.65

Table 4. *Cont.*

UT	Overall			Boundary		
	POLY	SH	SH-RBF	POLY	SH	SH-RBF
4	1.49	1.63	1.24	2.62	2.94	0.37
6	1.82	1.86	1.60	2.92	3.17	1.65
8	2.61	2.27	2.02	3.71	3.76	2.45
10	2.49	1.83	1.64	2.91	2.86	1.86
12	0.76	1.15	1.00	0.85	1.77	0.81
14	0.44	0.53	0.39	0.41	1.22	0.37
16	1.13	1.17	0.77	1.84	2.62	1.03
18	0.93	1.12	0.92	1.85	2.50	1.76
20	0.73	1.24	1.14	0.94	2.12	1.61
22	0.82	1.29	1.12	0.96	1.76	0.23

3.3. Analysis of Model Order and Modeling Accuracy

To quantitatively evaluate the impact of spherical harmonic model order on ionospheric modeling accuracy, this study applied third- and sixth-order spherical harmonic expansions to the same set of GNSS observation data. The overall and hourly RMSEs were calculated separately for geomagnetically active and quiet periods, and the results are shown in Figure 13.

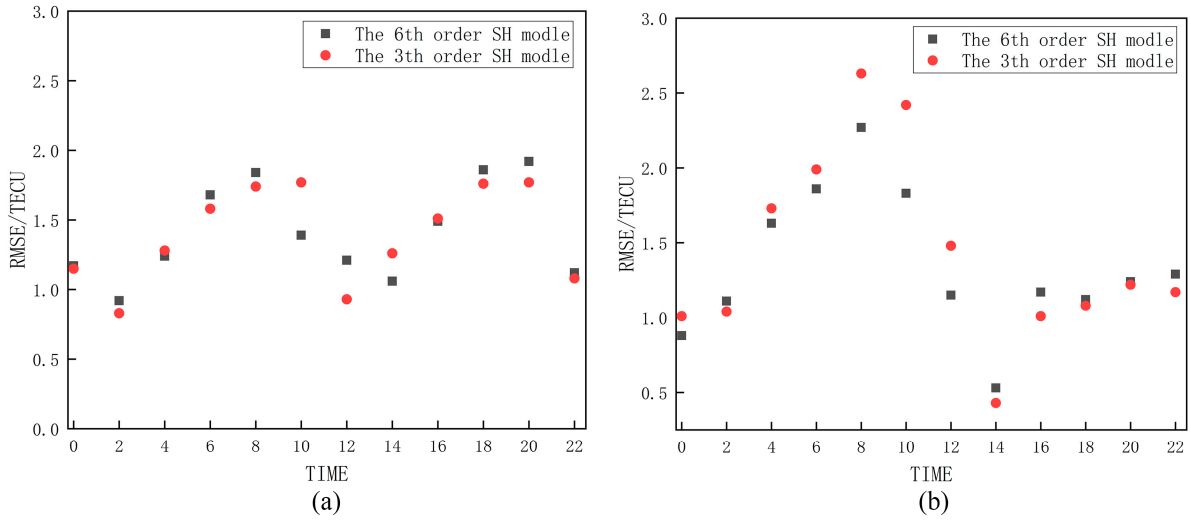


Figure 13. Distribution of RMSE for Spherical Harmonics of Different Orders. (**a**) geomagnetically quiet periods. (**b**) geomagnetically active periods.

During geomagnetically quiet periods, the third-order model shows a slight advantage in terms of overall RMSE. However, time series analysis reveals that the sixth-order spherical harmonic model achieves higher accuracy than the third-order model at certain local time points, such as UT 14, when the ionosphere is relatively active.

Under geomagnetically active conditions, the higher-order model demonstrates a systematic advantage. The overall RMSE of the sixth-order spherical harmonic model is 1.42 TECu, lower than the 1.56 TECu of the third-order model. This result clearly indicates that higher-order models are necessary to capture ionospheric variations when the ionosphere is strongly disturbed. Time series analysis further shows that the sixth-order model maintains lower error levels during most periods.

4. Discussion

This study demonstrates that the proposed SH-RBF method achieves higher ionospheric modeling accuracy than traditional spherical harmonic and polynomial methods, with a particularly notable improvement at regional boundaries. The superior performance of the SH-RBF method can be attributed to its effective hybrid nature. It leverages the capacity of spherical harmonics to precisely describe large-scale, global ionospheric variations, while the incorporation of radial basis function interpolation adeptly captures complex, nonlinear relationships and sharp gradients in boundary regions. This synergy between global and local modeling ultimately enhances overall ionospheric modeling accuracy.

4.1. Error Source Analysis

Estimation errors in differential code biases (DCBs) are a potential source of systematic error in the process of ionospheric modeling. Although this study addressed the rank deficiency of the normal equations by constraining the sum of all satellite DCBs to zero, and the estimated values are highly consistent with IGS products, residual DCB errors that are not fully absorbed during the solution process—particularly short-term fluctuations in receiver hardware delays during geomagnetically active periods—can still be transmitted to the VTEC estimates as systematic biases.

GNSS observation data serve as the raw material for ionospheric modeling, and the quality of the observations directly affects the modeling accuracy. Multipath effects and receiver internal noise in the original GNSS observations can degrade the signal-to-noise ratio of some data. Although carrier phase smoothing is applied, residual errors may still be introduced into the STEC as random noise. These errors may result in high-frequency fluctuations in the model fit that are difficult to explain by physical mechanisms. The distribution of ionospheric stations also has an impact on the modeling results. In this study, the selected stations are sparsely distributed at the edges of the study area but are evenly distributed in the central region. In areas where the distribution of stations is sparse or highly uneven, RBF interpolation may devolve into extrapolation due to insufficient local constraints, potentially limiting its correction performance. In such cases, the overall performance of the model becomes more sensitive to the coverage density of the IPPs.

4.2. Selection of Optimal Model Order

During geomagnetically quiet periods, the ionosphere is primarily influenced by solar radiation and exhibits large-scale, smooth gradient variations over time. Such structures can be adequately represented by low-order spherical harmonic functions. However, when geomagnetic storms occur, the substantial energy input at high latitudes triggers a series of dynamic processes, such as the generation of large-scale traveling ionospheric disturbances (TIDs). These processes introduce abundant sub-global-scale and mesoscale irregularities into the ionosphere. The order of the spherical harmonic functions essentially determines the spatial wavelength that the model can resolve. Therefore, during geomagnetically active periods, higher-order models are necessary to accurately characterize the state of the ionosphere.

In the ionospheric modeling process, the Dst and Kp indices are used to determine the level of geomagnetic activity, and higher-order models should be adopted during active periods. As shown in Figure 13a, the third-order spherical harmonic model achieves higher modeling accuracy than the sixth-order model during geomagnetically quiet periods. However, at certain epochs, such as UT14, the sixth-order model performs better, which may result from increased ionospheric activity due to solar radiation at those times. In Figure 13b, the improvement in the accuracy of the third-order model after UT14 likely

corresponds to an actual decline in geomagnetic activity, leading to a simplified ionospheric structure and thereby reducing the relative advantage of the higher-order model.

During geomagnetically active periods, acoustic-gravity waves (AGWs) can trigger traveling ionospheric disturbances. As key mediators between the lower atmosphere and the ionosphere [35], AGWs are the main physical mechanism responsible for the widespread occurrence of TIDs in the ionosphere. Therefore, in addition to the aforementioned errors affecting ionospheric modeling accuracy, actual physical processes in the Earth system are also important sources of residuals in the modeling results.

4.3. Future Prospects

In subsequent research, in order to further improve the accuracy of ionospheric modeling, we will enhance the quality of the data used for modeling by excluding observations with low signal-to-noise ratios. In addition, we plan to select study areas with different spatial scales and investigate the optimal model coefficients for each region under various geomagnetic conditions. Ultimately, our goal is to develop an adaptive ionospheric modeling system capable of real-time response to space weather dynamics.

5. Conclusions

This study proposes an innovative Spherical Harmonic–Radial Basis Function method, which synergistically combines spherical harmonics and radial basis function interpolation to address the challenge of degraded accuracy at boundary regions in regional ionospheric modeling. In this hybrid approach, spherical harmonics are used to model the global-scale distribution of Total Electron Content, while radial basis function interpolation locally corrects errors caused by edge effects. Using GNSS data from Europe during geomagnetically quiet and active periods, and taking the CODE Global Ionospheric Map as a reference, the performance of the SH-RBF method was systematically evaluated in comparison to traditional SH and polynomial methods. The main findings of the study are summarized as follows:

(1) The SH-RBF method significantly improves modeling accuracy, especially in boundary regions where traditional methods are prone to distortion. During geomagnetically quiet periods, the overall accuracy of SH-RBF was on average 14.49% higher than the SH method, with an average improvement of 53.51% in edge areas. The most effective corrections were observed during daytime, reaching 87.14%, while nighttime improvements were lower, with a minimum of 24.06%. During geomagnetically active periods, POLY outperformed spherical harmonics; however, SH-RBF not only showed superior accuracy in most cases, but also demonstrated significantly enhanced robustness throughout the day.

(2) There is a clear relationship between the optimal order of spherical harmonics and the intensity of geomagnetic activity. Lower-order spherical harmonics suffice during quiet periods, whereas higher-order expansions are required during disturbed periods to resolve finer spatial scales.

(3) Geomagnetic activity has a significant impact on ionospheric morphology. During active periods, both the peak value of ionospheric total electron content increased from 11.39 TECu in quiet periods to 14.32 TECu in this dataset, and the duration of ionospheric activity was prolonged. This reflects the substantial influence of space weather on ionospheric distribution and diurnal variation.

The performance of the SH-RBF model depends to some extent on the density and uniformity of GNSS monitoring stations. In regions where stations are sparse or unevenly distributed, the effectiveness of RBF interpolation may be limited by extrapolation, potentially affecting the final accuracy of the model.

Author Contributions: Conceptualization of the manuscript idea: H.Y.; methodology and soft-ware: W.D. and X.Z.; writing—original draft preparation: W.D. and X.Z.; supervision and funding acquisition: H.Y. and W.D. All authors have read and agreed to the published version of the manuscript.

Funding: This research was funded by the National Natural Science Foundation of China (NO. 51868074), the Xinjiang Uygur Autonomous Region Natural Science Foundation (NO. 2022D01C55) and Key Research and Development Projects in Xinjiang (NO. 2022B03033-1), Xinjiang Key Laboratory of Building Structure and Earthquake Resistance (NO. XJDX1703).

Data Availability Statement: GNSS observation data from IGS is available at http://www.igs.gnsswhu.cn/index.php (accessed on 1 July 2025), and precise orbit products from GFZ are accessible at ftp://igs.ign.fr/pub/igs/products/mgex/ (accessed on 1 July 2025). DCB are accessible at ftp://igs.ign.fr/pub/igs/products/mgex/dcb/ (accessed on 1 July 2025), GIM products from CODE are accessible at http://ftp.aiub.unibe.ch/CODE/2019/ (accessed on 1 July 2025). The Dst index and Kp index are provided by the Space Environment Prediction Center are accessible at http://www.sepc.ac.cn/TEC_chn.php (accessed on 1 July 2025).

Acknowledgments: We thank IGS for providing GNSS data products, CODE for providing ionospheric GIM data, and the Space Environment Prediction Center for providing geomagnetic indices Dst and Kp.

Conflicts of Interest: The authors declare no conflicts of interests.

References

1. Wang, C.; Zhang, T.; Fan, L.; Shi, C.; Jing, G. A simplified worldwide ionospheric model for satellite navigation. *IEEE Trans. Aerosp. Electron. Syst.* **2021**, *58*, 391–405. [CrossRef]
2. Rovira-Garcia, A.; Ibáñez-Segura, D.; Orús-Perez, R.; Juan, J.M.; Sanz, J.; González-Casado, G. Assessing the quality of ionospheric models through GNSS positioning error: Methodology and results. *GPS Solut. J. Glob. Navig. Satell. Syst.* **2019**, *24*, 631–653. [CrossRef]
3. Montenbruck, O.; Steigenberger, P.; Khachikyan, R.; Weber, G.; Hugentobler, U. IGS-MGEX: Preparing the Ground for Multi-Constellation GNSS Science. *Espace* **2014**, *9*, 42–49.
4. Rizos, C.; Montenbruck, O.; Weber, R.; Weber, G.; Hugentobler, U. The IGS MGEX experiment as a milestone for a comprehensive multi-GNSS service. In Proceedings of the ION Pacific PNT Conference, Honolulu, Hawaii, 22–25 April 2013.
5. Lanyi, G.E.; Roth, T. A comparison of mapped and measured total ionospheric electron content using global positioning system and beacon satellite observations. *Radio Sci.* **1988**, *23*, 483–492. [CrossRef]
6. Yunbin, Y.; Jikun, O. A generalized trigonometric series function model for determining ionospheric delay*. *Prog. Nat. Sci.* **2004**, *14*, 1010–1014. [CrossRef]
7. Schaer, S. *Mapping and Predicting the Earth's Ionosphere Using the Global Positioning System*; Geodaetisch-Geophysikalische Arbeiten in der Schweiz; Institut für Geodäsie und Photogrammetrie: Zürich, Switzerland, 1999; Volume 59.
8. Yuan, Y.; Tscherning, C.C.; Knudsen, P.; Xu, G.; Ou, J. The ionospheric eclipse factor method (IEFM) and its application to determining the ionospheric delay for GPS. *J. Geod.* **2008**, *82*, 1–8. [CrossRef]
9. Kumar, D.J.R.K. Modeling and optimization of ionospheric model coefficients based on adjusted spherical harmonics function. *Acta Astronaut.* **2021**, *182*, 286–294. [CrossRef]
10. Liu, A.; Li, Z.; Wang, N.; Zhang, Y.; Krankowski, A.; Yuan, H. SHAKING: Adjusted spherical harmonics adding KrigING method for near real-time ionospheric modeling with multi-GNSS observations. *Adv. Space Res.* **2023**, *71*, 67–79. [CrossRef]
11. Cheng, J.; Zhao, G.; Zang, N.; Cheng, S.; Chen, S.; Yao, J. A novel piecewise linear transformation to moderate regional boundary effect on Real-Time regional ionospheric map (RT-RIM). *Measurement* **2024**, *236*, 13. [CrossRef]
12. Christovam, A.L.; Prol, F.S.; Jerez, G.O.; Hernández-Pajares, M.; Camargo, P.O. PPP at low latitudes with ionospheric model exclusively based on single frequency GNSS measurements. *Space Weather* **2023**, *21*, e2023SW003513. [CrossRef]
13. Xiong, B.; Pan, L. Impact of different receiver DCB correction methods on wide-area undifferenced slant ionospheric delay modeling for PPP-RTK. *Adv. Space Res.* **2025**, *76*, 6794–6809. [CrossRef]
14. Yang, J.; Zheng, K.; Liu, K. A novel slant ionospheric model for PPP-RTK by considering horizontal gradient discrepancies across stations. *Measurement* **2025**, *257*, 118888. [CrossRef]
15. Zhao, J.; Ren, B.; Wu, F.; Liu, H.; Li, G.; Li, D. TECX-TCN: Prediction of ionospheric total electron content at different latitudes in China based on XGBoost algorithm and temporal convolution network. *J. Atmos. Sol. Terr. Phys.* **2023**, *249*, 106091. [CrossRef]

16. Kaselimi, M.; Voulodimos, A.; Doulamis, N.; Doulamis, A.; Delikaraoglou, D. A causal long short-term memory sequence to sequence model for TEC prediction using GNSS observations. *Remote Sens.* **2020**, *12*, 1354. [CrossRef]
17. Tang, J.; Liu, C.; Yang, D.; Ding, M. Prediction of ionospheric TEC using a GRU mechanism method. *Adv. Space Res.* **2024**, *74*, 260–270. [CrossRef]
18. Li, W.; Zhu, H.; Shi, S.; Zhao, D.; Shen, Y.; He, C. Modeling China's Sichuan-Yunnan's ionosphere based on multichannel WOA-CNN-LSTM algorithm. *IEEE Trans. Geosci. Remote Sens.* **2024**, *62*, 5705018. [CrossRef]
19. Tang, J.; Liu, C.; Hu, M.; Xu, L.; Ding, M.; Xu, C. Research on GNSS ionospheric forecasting in China based on the BiLSTM-GRU-Attention model. *Adv. Space Res.* **2025**, *76*, 7031–7043. [CrossRef]
20. Aa, E.; Huang, W.; Yu, S.; Liu, S.; Shi, L.; Gong, J.; Chen, Y.; Shen, H. A regional ionospheric TEC mapping technique over China and adjacent areas on the basis of data assimilation. *J. Geophys. Res. Space Phys.* **2015**, *120*, 5049–5061. [CrossRef]
21. Bergeot, N.; Chevalier, J.M.; Bruyninx, C.; Pottiaux, E.; Aerts, W.; Baire, Q.; Legrand, J.; Defraigne, P.; Huang, W. Near real-time ionospheric monitoring over Europe at the Royal Observatory of Belgium using GNSS data. *J. Space Weather Space Clim.* **2014**, *4*, a31. [CrossRef]
22. Li, Z.; Yuan, Y.; Wang, N.; Hernandez-Pajares, M.; Huo, X. SHPTS: Towards a new method for generating precise global ionospheric TEC map based on spherical harmonic and generalized trigonometric series functions. *J. Geod.* **2015**, *89*, 331–345. [CrossRef]
23. Rius, A.; Ruffini, G.; Cucurull, L. Improving the vertical resolution of ionospheric tomography with GPS Occultations. *Geophys. Res. Lett.* **2013**, *24*, 2291–2294. [CrossRef]
24. Nayak, K.; Romero-Andrade, R.; Sharma, G.; Colonna, R. Sequential Evolution of Ionospheric TEC Anomalies and Acoustic-Gravity Wave Precursors Associated with the February 8, 2025, Mw 7.6 Cayman Islands Earthquake. *J. Atmos. Sol. Terr. Phys.* **2025**, *274*, 106582. [CrossRef]
25. Schaer, S.; Steigenberger, P. Determination and use of GPS differential code bias values. In Proceedings of the IGS Workshop, Darmstadt, Germany, 8–12 May 2006.
26. Ren, X.; Chen, J.; Li, X.; Zhang, X. Multi-GNSS contributions to differential code biases determination and regional ionospheric modeling in China. *Adv. Space Res.* **2020**, *65*, 221–234. [CrossRef]
27. Wang, C.; Shi, C.; Fan, L.; Zhang, H. Improved Modeling of Global Ionospheric Total Electron Content Using Prior Information. *Remote Sens.* **2018**, *10*, 63. [CrossRef]
28. Doğanalp, S.; Köz, İ. Investigating Different Interpolation Methods for High-Accuracy VTEC Analysis in Ionospheric Research. *Atmosphere* **2024**, *15*, 986. [CrossRef]
29. Hardy, R.L. Multiquadric equations of topography and other irregular surfaces. *J. Geophys. Res.* **1971**, *76*, 1905–1915. [CrossRef]
30. Ma, L.; Wu, Z. Stability of multiquadric quasi-interpolation to approximate high order derivatives. *Sci. China Math.* **2010**, *53*, 985–992. [CrossRef]
31. Amoroso, P.P.; Aguilar, F.J.; Parente, C.; Aguilar, M.A. Statistical Assessment of Some Interpolation Methods for Building Grid Format Digital Bathymetric Models. *Remote Sens.* **2023**, *15*, 2072. [CrossRef]
32. Fasshauer, G.E. Newton iteration with multiquadrics for the solution of nonlinear PDEs. *Comput. Math. Appl.* **2002**, *43*, 423–438. [CrossRef]
33. Rippa, S. An algorithm for selecting a good value for the parameter c in radial basis function interpolation. *Adv. Comput. Math.* **1999**, *11*, 193–210. [CrossRef]
34. Sardón, E.; Zarraoa, N. Estimation of total electron content using GPS data: How stable are the differential satellite and receiver instrumental biases? *Radio Sci.* **1997**, *32*, 1899–1910. [CrossRef]
35. Kaladze, T.; Pokhotelov, O.A.; Shah, H.; Khan, M.; Stenflo, L. Acoustic-gravity waves in the Earth's ionosphere. *J. Atmos. Sol. Terr. Phys.* **2008**, *70*, 1607–1616. [CrossRef]

Disclaimer/Publisher's Note: The statements, opinions and data contained in all publications are solely those of the individual author(s) and contributor(s) and not of MDPI and/or the editor(s). MDPI and/or the editor(s) disclaim responsibility for any injury to people or property resulting from any ideas, methods, instructions or products referred to in the content.